Catalysis Today 358 (2020) 303–315

Contents lists available at ScienceDirect

Catalysis Today

journal homepage: www.elsevier.com/locate/cattod

Fischer-Tropsch studies in a 3D-printed stainless steel microchannel microreactor coated with cobalt-based bimetallic-MCM-41 catalysts

Nafeezuddin Mohammad[a], Richard Y. Abrokwah[b], Robert G. Stevens-Boyd[a], Shyam Aravamudhan[a], Debasish Kuila[a,b,*]

[a] Department of Nanoengineering, Joint School of Nanoscience and Nanoengineering, Greensboro, NC, 27411, USA
[b] Department of Chemistry, North Carolina A&T State University, Greensboro, NC, 27411, USA

ARTICLE INFO

Keywords:
MCM-41
Fischer-Tropsch synthesis
Synfuels
3D-printing
Stainless steel microreactor
Co-bimetallic catalysts

ABSTRACT

Fischer-Tropsch (FT) synthesis was carried out using 3D-printed stainless steel (SS) microreactors, containing channels of dimensions 500 μm × 500 μm × 2.7 cm, to study the effect of Fe, Ru, and Ni on Co-MCM-41 catalyst. The mono and bimetallic cobalt-based catalysts: 15 % Co-MCM-41, 10 %Co5% Ru MCM-41, 10 %Co 5%Ni MCM-41, and 10 %Co 5%Fe MCM-41 were synthesized using one-pot hydrothermal method and characterized by SEM-EDX, TEM, TPR, FTIR, XPS, and low and wide angle XRD techniques. All the catalysts exhibited high surface area without the loss of ordered mesoporous structure as confirmed by large BET surface areas (400- 1000 m^2/g) and low angle XRD data. The metal nanoparticles were in the range of 35 − 50 nm and well dispersed in a hexagonal matrix of MCM-41. TPR data indicate that all other metal oxides except that of cobalt can be reduced with H_2 below 600 °C. Cobalt is present most likely as cobalt silicates that can only be reduced with H_2 at a temperature over 650 °C. The microchannels of SS reactor were uniformly coated by dip coating a slurry of the catalyst with polyvinyl alcohol (PVA). The catalytic performance for FT synthesis was carried out in the SS microreactor at atmospheric pressure in the temperature range of 180–300 °C with H_2/CO molar ratio of 3. Incorporation of the second metal in the Co-MCM-41 framework and the operating temperature had a significant effect on CO conversion and selectivity towards C_1-C_4 alkanes in FT synthesis. While the highest CO conversion of 74 % was obtained for CoFe-MCM-41 at 240 °C, the highest selectivity towards butane (11 %) and propane (39 %) was observed for CoRu-MCM-41 at 240 °C and CoFe-MCM-41 at 210 °C, respectively. The rate of deactivation of the catalysts -followed the order: CoRu-MCM-41 > CoNi-MCM-41 > Co-MCM-41 > CoFe-MCM-41, indicating that CoFe-MCM-41 is the most suitable catalyst for F–T synthesis in terms of long term stability.

1. Introduction

In recent years, in the petroleum industry, alternative fuel sourcing has gained immense attention for research due to depletion of non-renewable energy sources such as fossil fuels. In order to overcome this problem, many chemical processes are currently being investigated. Fischer-Tropsch (FT) synthesis, which collectively refers to syngas conversion to synthetic crude oil, is an excellent chemical process for converting syngas to alkanes. Although Franz Fischer and Hans Tropsch discovered FT synthesis in the 1920s in Germany, it still remains one of the attractive topics for energy. In the FT process, syngas, a mixture of carbon monoxide and hydrogen, forms a monomer -CH_2 - that undergoes a polymerization reaction to form longer chains of alkanes as shown below. The water produced in the first reaction influences the exothermic water gas shift reaction and it plays an important role in the formation of H_2 and thus in the formation of alkanes.

$$nCO + (2n + 1)H_2 \rightarrow H(CH_2)H + n\,H_2O \qquad (1)$$

$$CO + H_2O \rightarrow (CO_2) + H_2\ \Delta\mathrm{H} = -41\ \mathrm{kJ/mol} \qquad (2)$$

FT process is an alternative route to produce environmentally friendly liquid fuel from any carbon sources like coal (coal-to-liquids (CTL)), natural gas or offshore gas (gas-to-liquids (GTL)), and biomass (biomass-to-liquids(BTL)) [1]. South Africa, which has large coal reserves, still continues to use coal-based FT synthesis. Recently, Sasol and Shell have commissioned large plants for natural gas-based FT synthesis in Qatar in 2006 and 2011, respectively [2]. The main FT reaction is temperature sensitive and highly restricted by exothermic heat produced during the reaction (heat released ∼ 140 − 160 kJ/mol CO converted), and is quite difficult to control the product selectivity in conventional reactors [3,4].

---

[*] Corresponding author at: Department of Chemistry, North Carolina A&T State University, Greensboro, NC, 27411, USA.
E-mail address: dkuila@ncat.edu (D. Kuila).

https://doi.org/10.1016/j.cattod.2020.02.020
Received 11 March 2019; Received in revised form 21 January 2020; Accepted 19 February 2020

The microreactor technology, containing microstructures with large surface to volume, provides an alternative platform for controlling an exothermic reaction with enhanced mass transfer and heat transfer and has gained a wide range of attention in process intensification [5] of FT synthesis [6]. A microreactor maintains isothermal operating conditions quite easily, favoring quick screening of a catalyst. The core of microreactors contains microchannels with smaller geometry having several parallel channels as a reaction zone. These microchannels enhance the specific surface area of the reactor resulting in an efficient FT synthesis. In addition to efficient heat and mass transfer with good heat dissipation, microreactors also have advantages for high reaction throughput, easy scale-up, good portability and lower cost over conventional reactors [6–10]. In general, the catalyst is loaded into a microreactor by packing and coating methods [11]. In the packing method, a catalyst is completely filled into the channels so that the spent catalyst is easily exchanged with the fresh catalyst. This is proven to be an effective technique and is now commercialized by Velocys Corporation [12]. While scaling these microunits, the pressure drop may be the biggest challenge as the length of the channel increases, thus making it difficult to control the temperature inside the reaction zone resulting in heat dissipation [13].

For German Normal-Pressure FT synthesis, the reactions were carried out at 1 atm using kieselguhr-supported Co-LTFT (low temperature FT) catalyst where kieselguhr is a natural high surface area silica that is not mechanically very strong [14]. In general, the FT reactions are usually carried out at much higher pressure. For gas phase reactions in FT synthesis, the active sites of the coated catalyst come in direct contact with the surface of the reactor leading to less pressure drop unlike packing methods [15,16]. The wall coated microreactors show high suitability for catalyst development to produce hydrocarbons from syngas, and it is simple for scaling up to pilot plants. In our previous studies to screen and develop catalysts for the FT synthesis, silicon was used to design and manufacture microreactors using microfabrication techniques [17–19] and the reactions were carried out at 1 atm. The fabrication of microchips on silicon wafer requires large fabrication infrastructure [20] and optimization in every fabrication step like deposition, photolithography, and deep reactive ion etching with high manufacturing costs. Additionally, it is challenging to create a leak-proof environment for gas phase FT reactions at higher temperature and pressure, as these reactions are usually carried out at a pressure of 20 bar or more to liquify the hydrocarbons. Furthermore, limits on the selection of gaskets to withstand higher temperatures and requirement of advanced torque-controlled reactor assembly without breaking Si microreactors are significant issues towards the development of a viable Gas-to-Liquid Technology (GTL). To address these limitations and challenges, microreactors fabricated using additive manufacturing methods have gained much research interest as they offer less complexity, more automation, and faster manufacturing processes [21,22]. Recently, 3D-printed microreactors have been used to study different chemical processes [23–26]. A few studies have also been reported for FT synthesis in stainless steel microreactors as they are known to be economical with good mechanical and thermal properties [11,27–29]. However, a microreactor with a smaller feature size have not been extensively investigated. In this study, a 3D-printed stainless steel microdevice (500 μm feature size) is fabricated using a design created in AutoCAD. Without the need of other manufacturing processes, this design yields a final 3D structure using a layer-by-layer technique and was used subsequently for FT synthesis.

FT synthesis depends on the number of active catalyst sites, thereby requiring support material with high surface area and good metal ion dispersion [30]. Therefore, the selection of support material with appropriate metal ion plays a vital role in syngas conversion. Some of the previous studies examined the role of Al_2O_3 [31–35], TiO_2 [11,36–42], SiO_2 [43–47] and CNTs [48–50] as supporting materials on the formation of higher alkanes.

In our previous studies, high surface area mesoporous silica such as MCM-41 supported catalysts were synthesized by one-pot procedure and was found to be extremely stable for steam reforming of methanol to produce H_2 [20,51–53]. The stability studies of MCM-41 catalysts motivated us to use MCM-41 as the support material for F–T synthesis and also to investigate any synergistic effect of a second metal ion on Co-MCM-41 for CO conversion and selectivity towards hydrocarbons. In this current study, three types of cobalt-based bi-metallic mesoporous silica support (MCM-41) and cobalt-MCM-41 were chosen to study the effect of bi-metallic systems of Co and M (Ru, Fe, and Ni) on FT synthesis. These catalysts were screened for FT synthesis in 3D-printed stainless steel microreactor. We also analyzed the interaction between support material and the metals in detail and discussed the most important factors that influence the performance of the catalyst for FT synthesis.

2. Experimental section

2.1. Materials and methods

The reagents used for catalysis synthesis were of analytical grade with no further purification. Tetraethyl orthosilicate, 99 % (TMOS) and ammonium hydroxide, ACS (American Chemical society) reagents, were purchased from Acros Organics, New Jersey, USA. Cetyltrimethylammoniumbromide (CTAB), $Co(NO_3)_2.6H_2O$, $Ni(NO_3)_2{\cdot}6H_2O$, $RuCl_3{\cdot}xH_2O$, $Fe(NO_3)_3{\cdot}9H_2O$ were purchased from Sigma Aldrich. Ethanol (anhydrous) and acetone, ACS grade, were obtained from Fischer Scientific, New Jersey, USA.

2.2. Microreactor fabrication and packing

The microreactor and cover channel were designed in AutoCAD and fabricated using 3D metal printing technology. A schematic diagram of the microchannel and its cover plate is shown in Fig. 1a and b. This microreactor design is based on split and recombination principle with 11 microchannels of dimensions 500 μm × 500 μm ×2.7 cm, as FT reaction zone of the microreactor. Fig. 1c shows the 3D-printed microreactor fabricated by direct metal laser sintering (DMLS) at Proto Labs Inc. This device is placed in the custom-built microreactor block with graphite gasket to have a leak-proof system for flow of syngas from the inlet to the outlet.

2.3. Catalyst synthesis and loading into the microchannels

Cobalt-based bi-metallic nanocatalysts supported by MCM-41 were synthesized using a one-pot hydrothermal procedure. TMOS, CTAB, de-ionized water, and ethanol were used in a molar ratio of 1:0.13:130:20 respectively. The quantity of metal precursors was calculated based on the weight percentage of metal to be incorporated into the catalysts. Typically, the weighed surfactant (CTAB) was dissolved in de-ionized water at 30 °C and stirred until the solution becomes clear. A separate solution was prepared by dissolving metal precursors in ethanol and stirring approximately for 30 min. The dissolved metal solution was gently poured into the CTAB solution and stirred vigorously for 30 min. TMOS, the limiting reagent for this chemical synthesis, was added dropwise into the mixture while stirring continuously for another 30 min. To precipitate the metal hydroxides at a pH of 10, ammonium hydroxide was added dropwise to the solution under stirring. The mixture was then stirred for another 3 h, followed by aging for 18 h at 65 °C. The precipitate obtained was washed with de-ionized water until it reached a pH of 7, then rinsed with ethanol and filtered. The filtered material was dried in air for 24 h then dried in an oven at 110 °C for 24 h. This dried catalyst was calcined at 550 °C for 16 h with a heating rate of 2 °C/min to remove the CTAB surfactant. It was then cooled to room temperature at a rate of -2 °C/min. Four types of catalyst were synthesized with 10 % of cobalt and nickel/iron/ruthenium, each 5% on MCM-41 support, and 15 % Co on MCM-41 support. They are labeled as

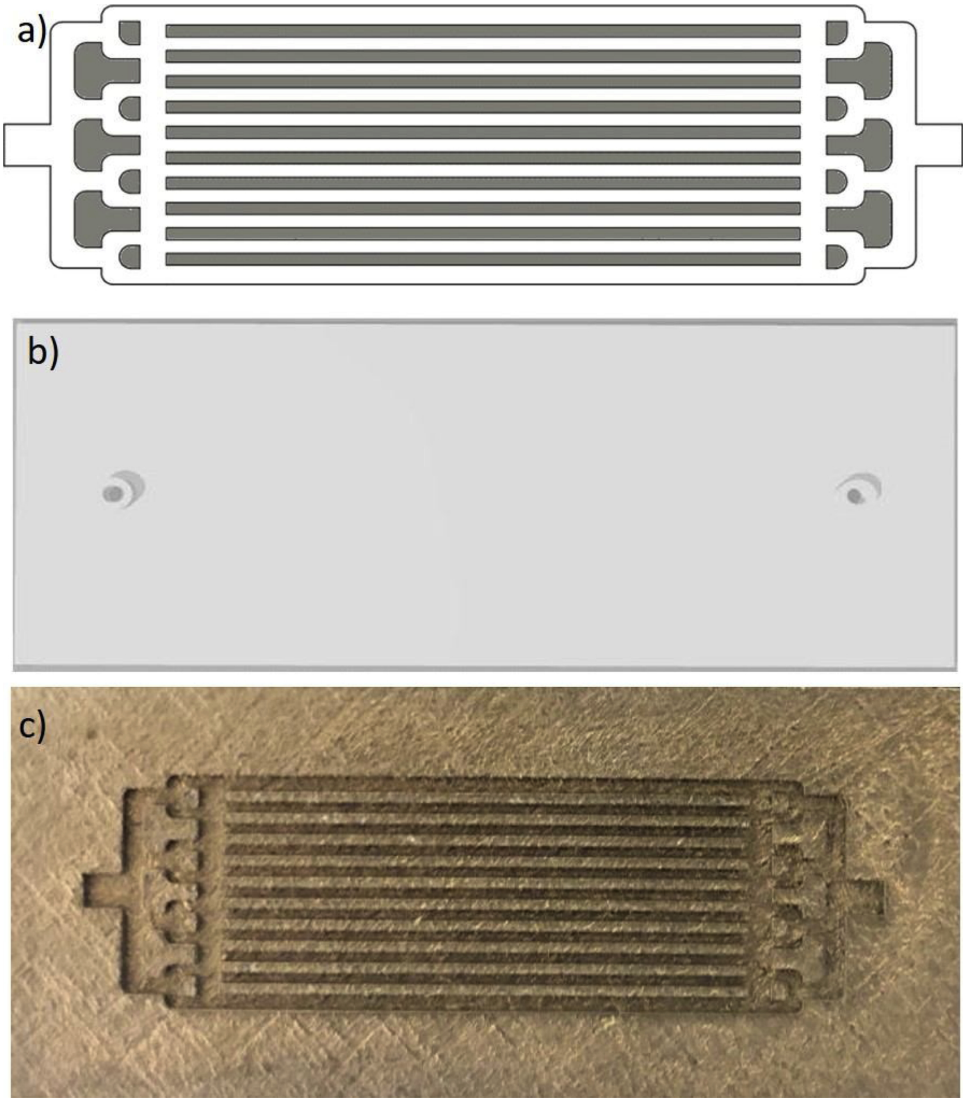

Fig. 1. a) and b) Schematic design of microreactor and cover channel respectively, c) 3D-printed microreactor.

CoNi-MCM-41, CoFe-MCM-41, CoRu-MCM41, and Co-MCM-41 for the rest of our discussion.

To load catalyst into the microchannels of the microreactor, each catalyst was immersed into a PVA suspension containing 4 g of Catalyst, 20 g of deionized water, 1 g of binder (polyvinyl alcohol 98–99 % hydrolyzed MW: 31,000 and 0.2 g of acetic acid. First, the PVA was dissolved in water with a low stirring rate at 60 °C for 2 h. The solution was then left covered for 12 h at room temperature. The catalyst powder and acetic acid were added successively to the binder solution and the resulting mixture was stirred for 2 h at 60 °C, and then at room temperature for a week. The microchannels of microreactor were dip-coated in the catalyst suspension and dried in air for 24 h and then calcined in presence of air for 2 h at 600 °C with heating and cooling rates of 5 °C/min. Fig. 2 shows the SEM image of uniformly coated microchannels with catalyst suspension after calcination.

2.4. Catalyst characterization

Specific surface area, pore size and pore volume of the synthesized catalyst were determined using a Micromeritics 3Flex instrument. The surface area was calculated using the Brunner-Emmett-Teller (BET) method which is typically an equation from adsorption isotherm with the relative pressure ranging from 0.07-0.3. The total volume was determined from N_2 adsorbed at $P/P_0 = 1$. The pore size distribution was calculated from the desorption of the nitrogen gas from the catalyst by using the BJH (Barret-Joyner-Halenda) method [54]. The H_2 temperature programmed reduction (TPR) and H_2 chemisorption analyses were done with the Mircomeritics 3Flex instrument with a TCD detector. A gas stream of 10 %H_2/Ar at a flow rate of 110 ml/min was passed through ~ 50 mg of catalyst, while the temperature was increased from room temperature to 1000 °C at 10 °C/min for TPR.

The Fourier Transform Infrared (FTIR) spectra were recorded using Shimadzu IR pressing Shimadzu IR Prestige-21 8300 spectrometer which has a mercury-cadmium-telluride (MCD) detector. The sample is prepared by the KBr pellet method. A very small quantity of catalyst sample is mixed with KBr in 1:200 wt ratio and grounded till the mixture becomes homogeneous using mortar and pestle. The mixture is then loaded into 13 mm die and pressed manually to form a pellet. The pellet is then mounted on the sample holder and the spectrum was recorded in the range of 4000 to 400 cm^{-1} resolution at room temperature.

The small and wide-angle powder x-ray diffraction (XRD) were recorded using a Rigaku SmartLab X-ray diffractometer with Cu K-α radiation (wavelength = 0.15418 nm) radiation generated at 40 mA and 40 kV. The step size and time per step used in these measurements are 0.05° and 3 s/step, respectively. The crystal sizes of the metal oxides

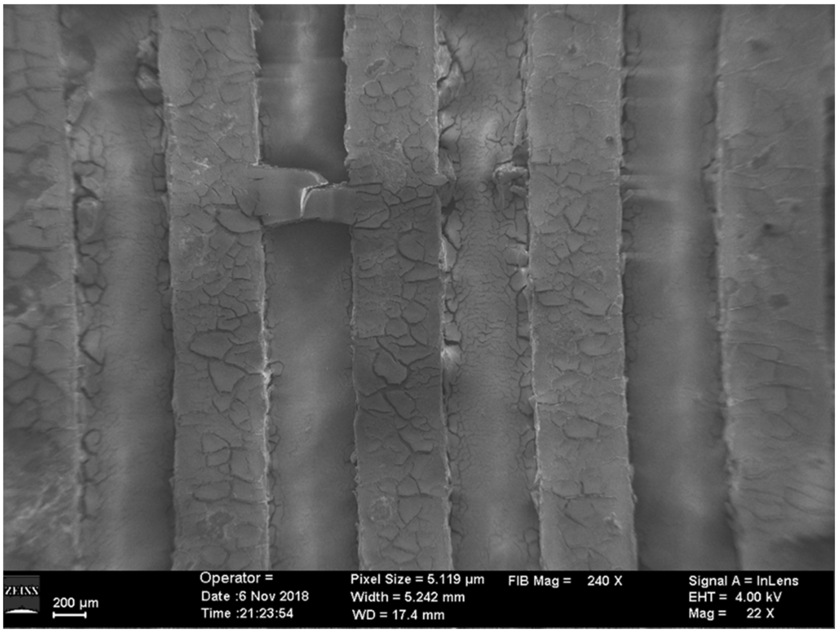

Fig. 2. SEM image of Microchannels uniformly coated by catalyst.

were determined using the Scherrer equation. In the Scherrer equation below, τ stands for the crystal size, λ is the wavelength of the Cu Kα radiation, β is the full width half maximum and θ is the Bragg diffraction angle.

$$\tau = \frac{0.9\lambda}{\beta^{*}\mathrm{Cos}\theta}$$

The morphology and the size of the catalysts were analyzed using transmission electron (TEM Carl Zeiss Libra 120) at 120 KeV and scanning electron microscopy (Zeiss Auriga FIB/FESEM). The elemental composition and transition states of metals were analyzed using Energy Dispersive X-ray spectrometry (Zeiss Auriga FIB/FESEM) and X-ray photon spectroscopy (XPS-Escalab Xi+-Thermo scientific), respectively.

The sample for TEM was prepared by dispersing a small quantity of catalyst in 3 ml of ethanol followed by vortex dispersion and sonication for a few minutes. Then a carbon-coated copper grid of 300 μm mesh size was drop coated by the suspension and then dried in an oven at 100 °C for 12 h.

2.5. Microreactor experimental setup for Fischer-Tropsch synthesis

The FT experiments were carried out in an in-house built LabVIEW automated experimental setup with precise control of the operating conditions. The experimental setup is shown in Fig. 3. The flow rate of the syngas mixture (H_2 & CO) was controlled by a precalibrated mass flow controller (Cole Parmer) with a maximum flow rate of 1 sccm. The carrier gas, nitrogen was controlled by a precalibrated mass flow controller (Aalborg) with a maximum flow of 10 sccm. The pressure on upstream and downstream was monitored continuously by Cole-Parmer pressure gauges from which the data was fed to an Aalborg solenoid valve. The entire setup was automated by the LabVIEW 2018 program. The products were analyzed by GC–MS Agilent Technologies 7890B GC and Agilent 5977 MSD system. Prior to experiments, the catalyst inside the microreactor was reduced *in-situ* at 350 °C overnight to compensate the losses in *ex-situ* reduction and oxidation of catalyst before reaction. The FT reaction was performed with syngas (H_2/CO) molar feed ratio of (0.9 sccm: 0.3 sccm) 3:1. The gas hourly space velocity (GHSV = v_0/V, where v_0 = the volumetric flow rate of feed at STP and V = Reactor volume) and the reaction pressure were maintained constant at ~ 6000 h^{-1} and 1 atm, respectively. The reaction temperature was varied between 180 °C and 300 °C at 30 °C interval, for each temperature a freshly reduced catalyst coated in microchannels of microreactor was introduced into the reactor block and reduced *in-situ* at 350 °C for 12 h to compensate for the oxidation loses while transferring the microreactor to the reaction line. Based on the preliminary runs, the reaction reached a steady state after 2 h of each set point temperature. Therefore, the conversion and selectivity were obtained after 3 h. Deactivation studies of the catalysts were also performed. The FT reaction deactivation studies were carried out at 240 °C using syngas feed molar ratio of 3:1.

The formulas for CO conversion and hydrocarbon selectivity calculated based on the carbon basis are shown below. The selectivity of CO_2 was not quantified in our calculations.

$$CO\ conversion\ (\%) = \frac{moles\ of\ CO_{in} - moles\ of\ CO_{out}}{moles\ of\ CO_{in}} \times 100$$

$$CH_4\ Selectivity\ (\%) = \frac{mCH_4}{mCH_4 + 2mC_2H_6 + 3mC_3H_8 + 4mC_4H_{10}} \times 100$$

$$C_2H_6\ Selectivity\ (\%) = \frac{2mC_2H_6}{mCH_4 + 2mC_2H_6 + 3mC_3H_8 + 4mC_4H_{10}} \times 100$$

$$C_3H_8\ Selectivity\ (\%) = \frac{3mC_3H_8}{mCH_4 + 2mC_2H_6 + 3mC_3H_8 + 4mC_4H_{10}} \times 100$$

$$C_4\,H_{10}\ Selectivity\ (\%) = \frac{4mC_4H_{10}}{mCH_4 + 2mC_2H_6 + 3mC_3H_8 + 4mC_4H_{10}} \times 100$$

3. Results and discussion

3.1. Textural properties evaluation of catalyst

To study the textural properties of the synthesized catalysts, nitrogen BET physisorption analyses were performed. The BET surface area, pore volume and average pore diameter of the catalysts are presented in Table 1. The surface areas of the catalyst were in the range of 1025 - 434 m^2/g, and the pore diameter was observed in the range of 3.2–5.1 nm depending on the type of metal incorporated in the MCM-41 matrix. Fig. 4a shows the nitrogen adsorption-desorption isotherms of all four samples. All the isotherms fall under the category of Type IV

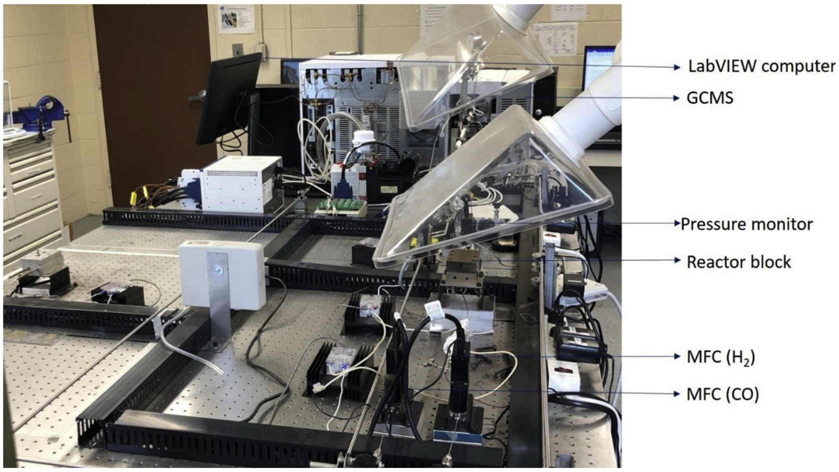

Fig. 3. Microreactor set up on the optical table.

Table 1
BET surface area, pore size and pore volume of synthesized catalyst.

MCM-41 Supported Catalyst	Surface Area[a] (m^2/g)	Pore volume[b] (cm^3/g)	Pore size[c] (nm)
CoRu-MCM-41	1025.3	0.77	3.2
Co-MCM-41	820.5	1.1	5.1
CoFe-MCM-41	574	0.54	3.7
CoNi-MCM-41	434	0.5	4.6

[a] = Variation range ± 2%.
[b] = Variation range ± 3%.
[c] = Variation range ± 5%.

isotherms which is typical for mesoporous materials according to the IUPAC classification [55]. This isotherm is classified into three regions. The initial part of the Type IV isotherms resembles Type II isotherm which is a linear increment in the nitrogen uptake at low relative pressures (P/P_0 = 0-0.2), contributing to monolayer-multilayer adsorption on the pore walls. At higher relative pressures (P/P_0 = 0.2 - 0.4), capillary condensation in the mesopores takes place. The steepness of this step-up region indicates narrow pore size distribution, which is shown in Fig. 4b. The sharpness of this peak in the isotherm is clearly seen, indicating an ordered mesoporous structure. The third region at relative pressures P/P_0 = 0.4 - 0.95, which is a long plateau, corresponds to multilayer adsorption on the outer surface. At relative pressures, $P/P_0 > 0.95$ a sharp increase in N_2 uptake associated with a hysteresis loop indicates condensation of N_2 in the interstitial voids of MCM-41 [56].

It should be emphasized that the mesoporous structure is not disrupted upon metal addition as indicated by the low angle XRD (discussed below) studies. Metal ions are bound to the pores of the support without disturbing the ordered mesoporous structure. The total pore volume was observed in the range around 1.1-0.5 cm^3/g for all the catalysts.

3.2. Low and wide angle XRD studies

Low angle XRD studies were carried out to obtain information about the structural polymorphs of the catalysts. Fig. 5 shows the diffraction patterns for all the catalyst samples. Small angle XRD patterns for all the catalyst showed variations of peaks probably due to the different type of metal nanoparticles present. A sharp intense peak between 2-theta value 2° - 3° and two broad peaks between 2-theta value 4°- 5.5° corresponds to (100), (110) and (200) reflections of hexagonal mesoporous structure. The intensity of peaks is observed to decrease or disappear with a decrease in surface area. This indicates the distortion of an ordered mesoporous structure because of the type of metal and its interaction with the MCM-41 matrix. The (100) reflections and very low intensity of (110) and (200) peaks for CoRu-MCM-41and Co-MCM-41 confirm that these catalysts are highly ordered mesoporous in nature with no noticeable effect on the hexagonal framework. The decrease in the peak intensity in case of CoNi-MCM-41 and Co-Fe-MCM-41 also implies that the metal atoms are highly dispersed into the MCM-41 framework having extremely small particle size < 3 nm which is beyond the X-ray detection limit [57].

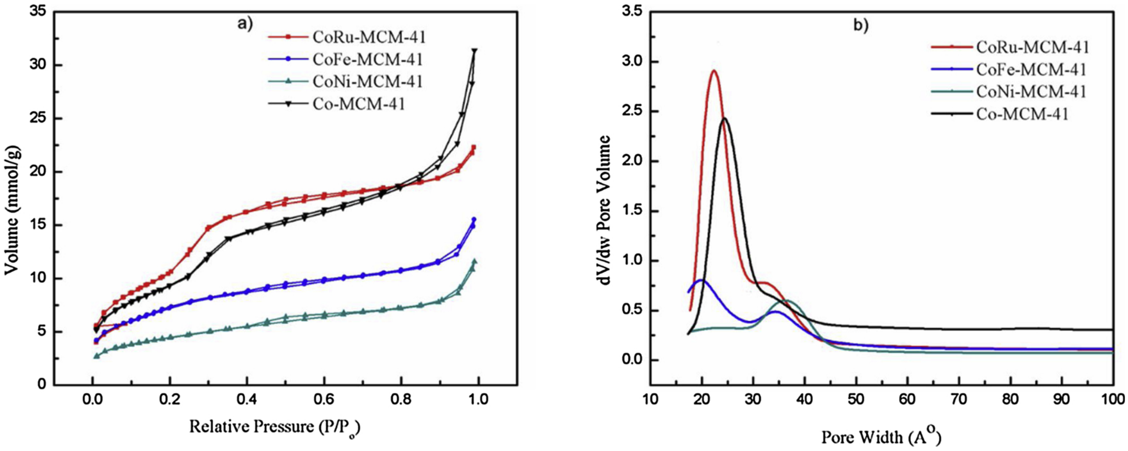

Fig. 4. a) N_2 adsorption-desorption isotherms of M-Co- MCM-41 and Co-MCM-41Catalysts (M = Fe, Ru, Ni) catalysts; b) pore size distribution of the catalyst.

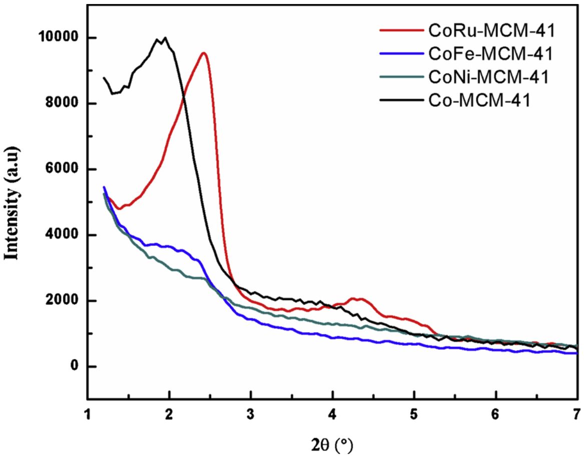

Fig. 5. Low angle XRD patterns of M-Co- MCM-41 and Co-MCM-41Catalysts (M = Fe, Ru, Ni).

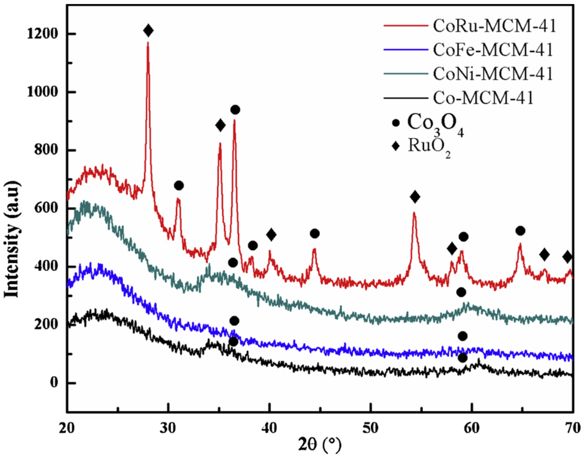

Fig. 6. Wide angle XRD patterns of M-Co- MCM-41 and Co-MCM-41Catalysts (M = Fe, Ru, Ni).

In order to know the crystal structure, wide-angle XRD analysis was carried out for different catalysts. Fig. 6 shows the X-ray diffraction patterns of different samples. The catalysts data are compared with the JCPDS (Joint Committee on Powder Diffraction Standards) database. In CoRu-MCM-41 sample, the peaks at 31.09° (220) and 59.05° (511) correspond to cubic structure Co_3O_4 (JCPDS-80-1534). The peaks at 36.54° (311), 38.24° (222) and 44.46° (400) belong to cubic structure Co_3O_4 crystal (JCPDS-80-1543). Another cubic structure of Co_3O_4 crystal (JCPDS-80-1535) is found at 64.71° (440). The tetragonal structure of RuO_2 (JCPDS-43-1027) is observed at 27.96° (110), 35.13° (101), 40.06° (200), 54.32° (211) and 57.96° (220). The peaks at 67.22° (112) and 69.72° (301) correspond to orthorhombic the structure of RuO_2 (JCPDS-88-0323). The Co_3O_4 peaks are also observed at 36.54° and 59.05° for other catalysts sample. In the other samples, no significant peaks for other metals is observed. This can be attributed to either high dispersion of metal nanoparticles into the MCM-41 hexagonal matrix or the metal particles are extremely small in size ($<$ 3 nm) which makes X-rays difficult to detect during the analysis [57].

3.3. SEM-EDX and dispersion analysis of the catalysts

The surface morphology and the concentration of metal nanoparticles (by wt%) that are encapsulated into the matrix were determined by SEM-EDX analysis. Fig. 7 shows the SEM images for Co-FeMCM-41 and CoRu-MCM-41 at high and low magnification. The high magnification images in Fig. 7a and c show that the catalyst samples exhibit regular sphere-shaped particles with a smooth surface morphology. Fig. 7b and c show the low magnification images of the catalyst containing uniform porous structure. Table 2 summarizes the intended metal loading and the actual metal loading with metal dispersion of the various catalyst samples. The intended weight percentage of the metal loaded into the MCM-41 support was consistent with the loadings determined from EDX analysis. The uniformity of metal ions distribution into the matrix is confirmed by EDX mapping shown in Fig. 8. The distribution of metal particles plays an important role in its stability. This is also confirmed by metal dispersion of catalysts ranging from 0.0452-0.0162 depending on the type of metal incorporated. The highest metal dispersions in the support are exhibited by CoRu-MCM-41 and Co-MCM-41; this indicates that the metal distribution is more uniform and highly ordered without affecting the structure of the support. This is consistent with the BET results showing highest surface area for CoRu-MCM-41 and Co-MCM-41. An uniform distribution of the catalyst avoids sintering in Fischer-Tropsch synthesis, thus avoiding the deactivation of catalyst in our studies.

3.4. Transmission electron microscopy (TEM)

TEM was performed to observe the pore and metal particle size of the synthesized catalysts. Fig. 9 shows low and high magnification images of CoRu-MCM-41 sample. The TEM image under high magnification shows clear and uniform ordered hexagonal pores of the MCM-41 matrix that is consistent with BET and XRD results. The low magnification shows the uniform distribution of particles that are observed in black dotted circular shapes in clear MCM-41 matrix.

3.5. FTIR studies of the catalysts

To understand the changes in the bonding properties and the metal ion interaction with the MCM-41 matrix, FTIR spectra were recorded. **Fig. S1** in the supplemental material shows the FTIR spectra of as-prepared MCM-41, Co-MCM-41 and the calcined samples of CoRu-MCM-41, Co-MCM-41. The as-prepared samples exhibit two peaks in the range of 2800 cm^{-1} - 3000 cm^{-1} and another peak at ∼1500 cm^{-1}. These absorption bands are assigned to symmetric C–H stretching and asymmetric $-CH_2$ - vibrations of the CTAB template. The disappearance of these peaks indicates that calcination completely removed the template. The broad absorption band in the region of 3000 cm^{-1} - 3700 cm^{-1} is assigned to the stretching of hydroxyl bonds and adsorbed moisture on the support [58,59]. Since MCM-41 is hydrophilic in nature tending to adsorb water molecule, a low-intensity band was seen around 1650 cm^{-1} that is associated with the bending vibrations of water molecules entrapped in the MCM-41 matrix [60]. The peaks observed between 800 cm^{-1} and 1000 cm^{-1} are due to the bending and symmetric stretching vibrations of Si-O-Si bonds [59,61]. The absorption bands observed at 1250 cm^{-1} and 1020 cm^{-1} are associated with the symmetric stretching vibrations, while the band at 800 cm^{-1} is due of the symmetric stretching vibrations of Si-O-Si links in the hexagonal matrix [62,63]. The absorption peaks around 500 cm^{-1} were attributed to the metals that are incorporated in the MCM-41 support, which could be associated with the bending vibrations of Si-O-Si links [64]. These results are similar to the data reported in our previous studies [20,53]

3.6. Chemical oxidation states of incorporated transition metals in MCM-41

The chemical states of the metals that are incorporated in the MCM-41 matrix were determined using X-ray photoelectron spectroscopy (XPS). Fig. S2 shows the spectra for Si 2p centered at 154 eV and O 1s centered at 533 eV for all the catalysts, which are characteristic values for the silicates. The Si 2p binding energy of 154 eV provides information about the link between Si-O in tetrahedral, SiO_4 units. Similarly, the binding energy for O 1s indicates that the atoms are

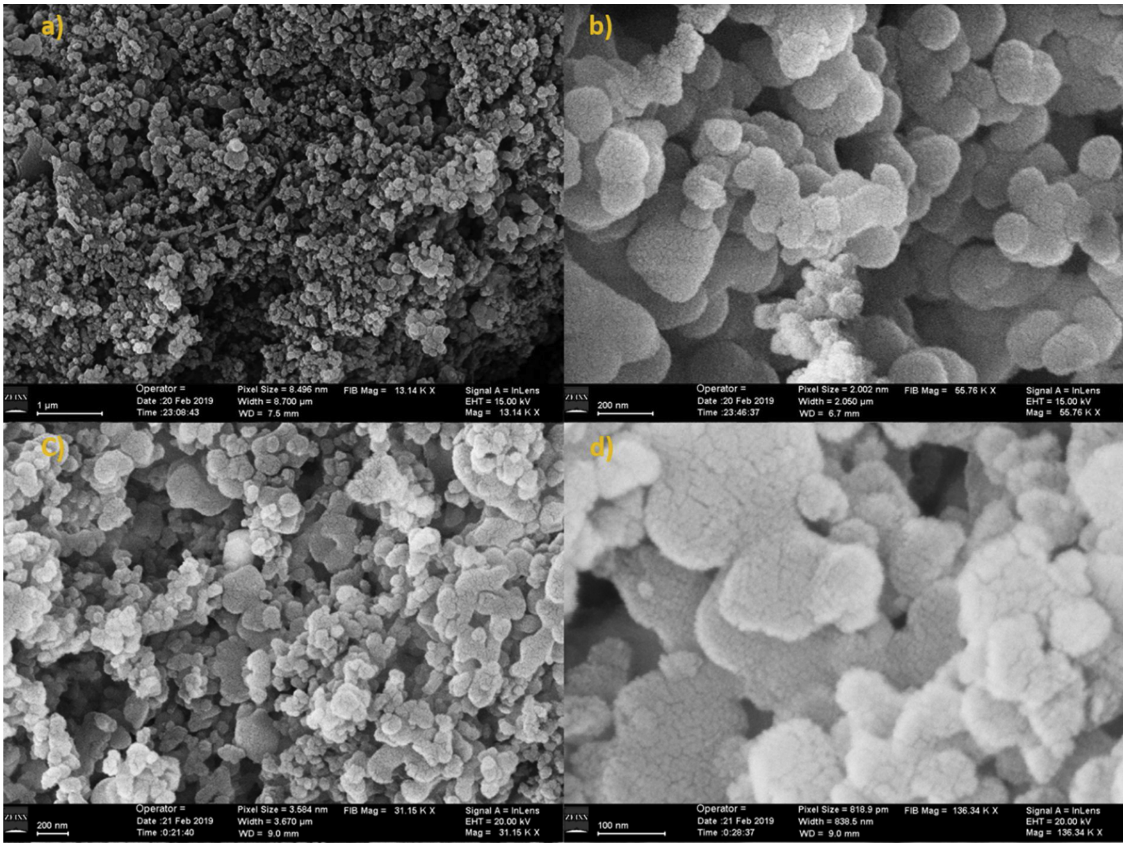

Fig. 7. Low and high magnification SEM images of CoFe-MCM-41 and CoRu-MCM-41 catalyst samples a) low magnification CoFe-MCM-41 b) high magnification: CoFe-MCM-41 c) low magnification CoRu-MCM-41 d) high magnification: CoRu-MCM-41.

Table 2
Metal Loading, M:Co atomic ratio and dispersion studies of Bimetallic Co-MCM-41 catalyst samples.

Catalyst with intended metal loading	Metal loading using EDX (wt %)	M: Co (M = Ru,Fe,Ni)	H_2 Chemisorption dispersion
10 %Co5%Ru-MCM-41	9%Co 3.9 %Ru-MCM-41	3.671135	0.0452
10 %Co5%Fe-MCM-41	10.2%Co 8%Fe-MCM-41	1.054636	0.0215
10 %Co5%Ni-MCM-41	9.1%Co 5.7 %Ni-MCM-41	1.301728	0.0162
15 %Co-MCM-41	14.33%Co-MCM-41	–	0.0497

strongly bonded in the Si-O links without a shift in the binding energy; similar results were reported by Shen et al., [57] and Sterczunska et al., [65]. Fig. 10a illustrates the X-ray photoelectron spectra of cobalt in all the samples. Two peaks are observed: one centering at ~782.5 eV associated with $2p_{3/2}$ and other centering at ~ 798 eV, associated with $2p_{1/2}$ which were due to Co 2p transition splits. The Co $2p_{3/2}$ in Co 2p spectra are assigned to Co^{2+} and suggests successful incorporation of Co^{2+} into the framework of MCM-41 [66]. For isolated cobalt, the binding energy values are observed at 779.6 eV and 795.6 eV for $2p_{3/2}$ and $2p_{1/2,}$ respectively. Thus, the significant shift to higher binding energy in our samples suggests a strong interaction between tetrahedral Co(II) with MCM-41 matrix. This is consistent with that reported by Shen et al. [57]. Fig. 10b, Fig. 10c and Fig. 10**d** show XPS spectra of Fe, Ni, and Ru. Fig. 10**c** shows two broad peaks centered at 713 eV and 725.7 eV for Fe $2p_{1/2}$ and $2p_{3/2}$. Similar spectra for Fe 2p were obtained by Shen and co-workers [57] and Stefainis and co-workers [67]. The Fe in CoFe-MCM-41 exists both in Fe^{2+} and Fe^{3+} states. Similarly, the Ni^{2+} $2p_{3/2}$ XPS spectra are obtained at 857.4 eV and it is shown in Fig. 10d. This shift when compared to the original Ni^{2+} $2p_{3/2}$ location is due to the strong Ni-O chemical bonds in MCM-41 matrix [68,69]. Fig. 10b shows the XPS spectra for Ru in CoRu-MCM-41 sample. The peak for CoRu-MCM-41 is not well defined and has low intensity; this may be due to very high BET surface area of the MCM-41 matrix and its resistance to the formation of bulk cobalt species [70,71]. The XPS spectra for Ru 3d and C 1s peaks overlap around 285 eV, making it difficult to confirm the presence of Ru 3d state in the sample; however, a peak around ~ 280 eV is clearly observed, which is associated with Ru 3d $_{5/2}$ as reported elsewhere [72].

3.7. Temperature programmed reduction(TPR) studies

Temperature programmed reduction (TPR) is one of the most convenient tools to study the reduction behavior of the metal oxide catalysts and evaluate the metal-support interactions [20,51]. The calcined catalysts are treated with 10 % H_2/Ar and the TPR profiles for the mono and all bimetallic cobalt-based samples are shown in Fig. 11. In all the samples, cobalt exhibits two very low-intensity peaks centering at almost 324 °C and 614 °C and a high-intensity peak centered approximately at 780 °C. The first two very low-intensity peaks correspond to the reduction of Co_3O_4 to CoO and CoO to Co°; the high-intensity peak attributes to reduction of cobalt hydro silicate to Co° [20,73–76]. The addition of Fe, Ru, and Ni metal ions resulted in disappearance of the low-intensity peaks. This could be due to suppression of cobalt -support interaction caused by Fe, Ni, and Ru ions [77]. The last peak centering at almost 780 °C inCo-MCM-41 suggests that the cobalt and the MCM-41 matrix have strong interaction [77–79]. We speculate the formation

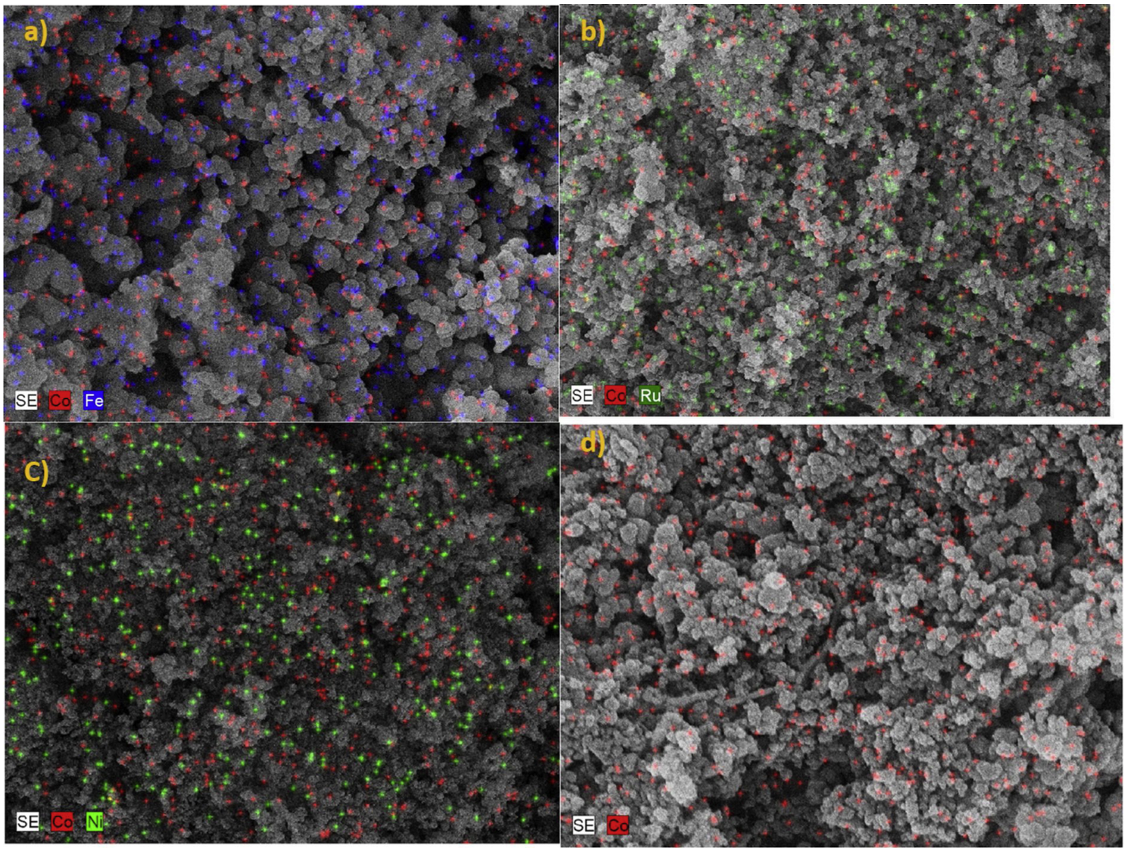

Fig. 8. SEM-EDX images of different catalyst samples: a) CoFe-MCM-41 b) CoRu-MCM-41 c) CoNi-MCM-41 d) Co-MCM-41.

of cobalt silicates containing a spinel structure that can only be reduced at a temperature above 750 °C. In bimetallic- catalysts, the ease of reducibility of the other metal oxide and replacement of the cobalt ion with other metals tend to shift the reduction peaks to a lower temperature. Thus, the metal and support interaction has great influence on the reducibility and reactivity of the catalyst in FT synthesis. The catalyst activity mainly depends on the ease of reduction of metals at reaction operating conditions.

Reduction of RuO_2 to Ru° occurs at a much lower temperature than that observed in Co_3O_4. It occurs in two steps as indicated by the peaks centering at almost 207 °C and 271 °C in CoRu-MCM-41 catalyst. Similar results are demonstrated by Bentancourt et al., [80,81]. A broad peak for CoFe-MCM-41 is observed in the temperature range of 300 °C–450 °C and suggests reduction of Fe in CoFe-MCM-41 catalyst [82,83]. For CoNi-MCM-41, NiO is reduced at lower temperature ~ 380 °C and a broad peak overlying with Co silicates is seen ~ 600 °C

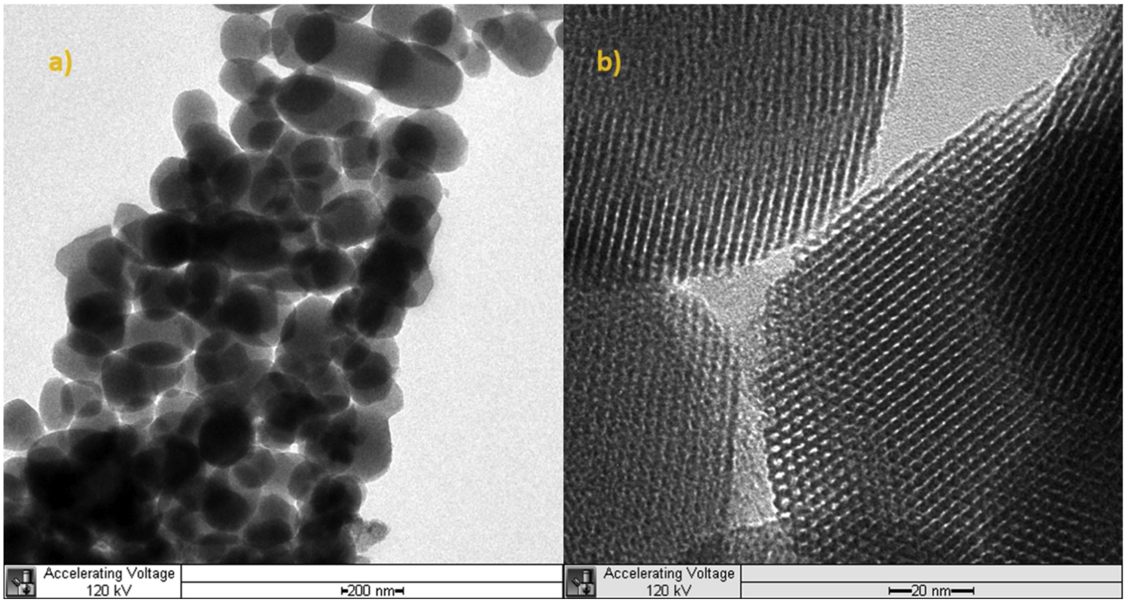

Fig. 9. TEM image of CoRu-MCM-41 catalyst sample: a) low magnification b) high magnification.

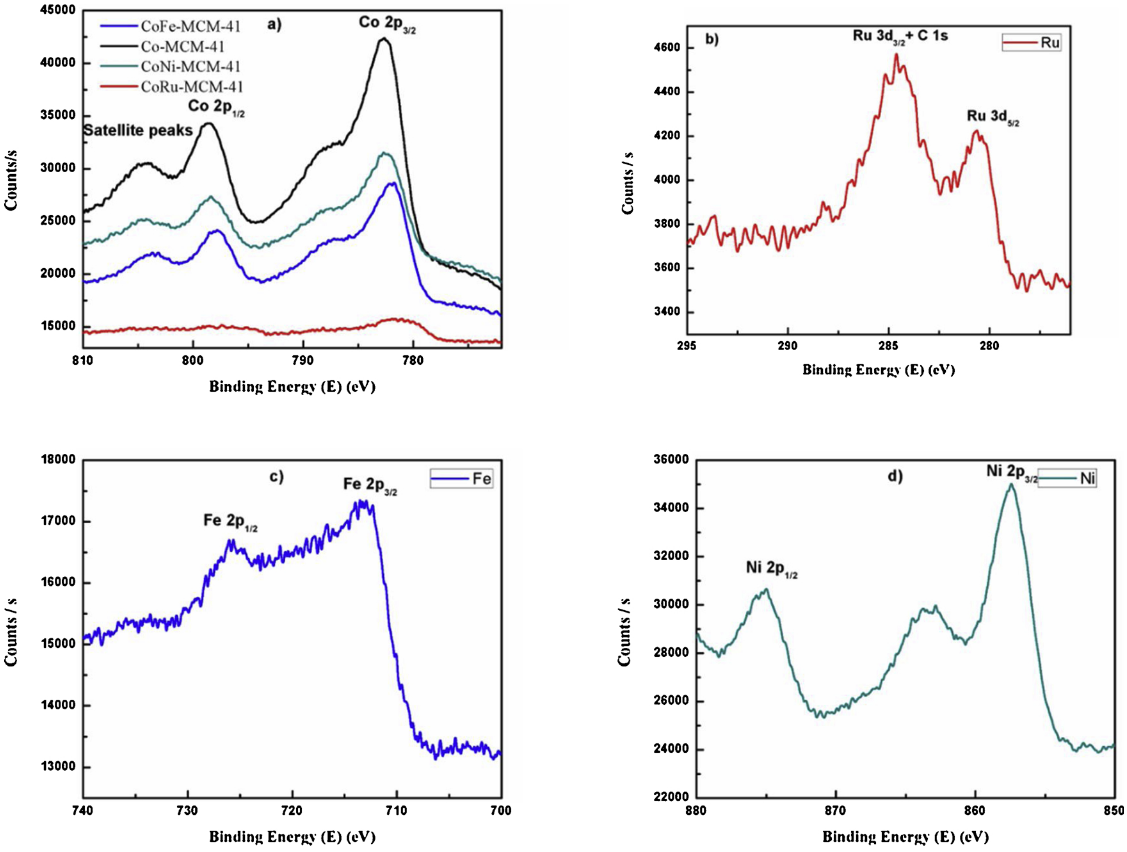

Fig. 10. XPS spectra of metal incorporated MCM-41 a) Co 2p b) Ru 3d c) Fe 2p d) Ni 2p.

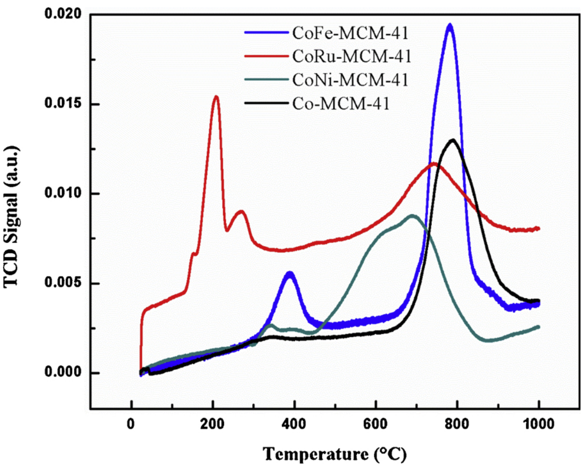

Fig. 11. H_2-TPR profiles of M-Co- MCM-41 and Co-MCM-41Catalysts (M = Fe, Ru, Ni).

that can be associated with Ni silicates. [84,85]. In all the samples after incorporation of Ru, Fe and Ni ions into the MCM-41 support, the reduction peaks are observed at higher temperatures. It is also observed that there is a decrease in the reduction peak of Co-silicates indicating the formation of oxo-bridged Co-O-M (M = Fe, Co, Ni) structure, which is stabilizing the cobalt ion in the support. These results are consistent with the shift in the XPS spectra of the metal ions.

3.8. *Fischer-Tropsch activity of the catalysts*

All the catalysts were tested for Fischer-Tropsch studies at H_2: CO molar flow (3:1) and at different reaction temperature (T = 180, 210, 240, 270, 300 °C) with the constant pressure of 1 atm and ∼6000 GHSV. GHSV was calculated as the flow rate at standard temperature and pressure per unit volume of the catalyst. The weight of the catalyst coated in the microchannel reactor was ∼ 0.0033 g, obtained by the difference in the weights of the microchannel microreactor before and after coating and calcination under air. Prior to the reaction with metal loaded catalysts, FT synthesis was carried out with simple MCM-41 support (only) coated in stainless steel microreactor. Neither CO conversion nor hydrocarbon selectivity were observed when the reaction was carried out at 240 °C at 1 atm with fixed H_2: CO (3:1) molar ratio. Our studies show that support MCM-41 is inert and does not have any intrinsic effect in FT synthesis. Furthermore, the SEM image in Fig. 2 shows that the surface of the microreactor is fully coated with the catalyst with no exposure of stainless-steel material to the reaction zone for FT synthesis. A similar coating method was used to obtain SEM images in our previous studies to investigate the effect of mesoporous silica (MCM-41, SBA-15 and KIT-6) on the kinetics of catalyst for FT synthesis at 1 atm [86].

The effect of reaction temperature on CO conversion and selectivity of Co-MCM-41 and CoRu-MCM-41 are shown in Fig. 12. For all the samples, conversion of CO showed an almost similar trend with an increase in the temperature. The selectivity of the catalyst changed with temperature and type of the metal ion incorporated with cobalt in the MCM-41 support using one pot procedure [20]. For example, Co-MCM-41 exhibited the highest selectivity towards propane and butane, 9.27 % at 210 °C and 7.95 % at 240 °C respectively with 64.5 % CO conversion at 240 °C. The effect of temperature on CoFe-MCM-41 and CoNi-MCM-41 catalysts towards the hydrocarbon selectivity and the conversion is shown in Fig. 13. The low selectivity towards C_1-C_4 is possibly due to strong interaction of the Co ion with the MCM-41 matrix forming very stable cobalt silicates that cannot be reduced easily. This is reflected in TPR studies where reduction of Co-oxide and silicates is observed > 750 °C. The Co-MCM-41 catalyst has yielded a lot of

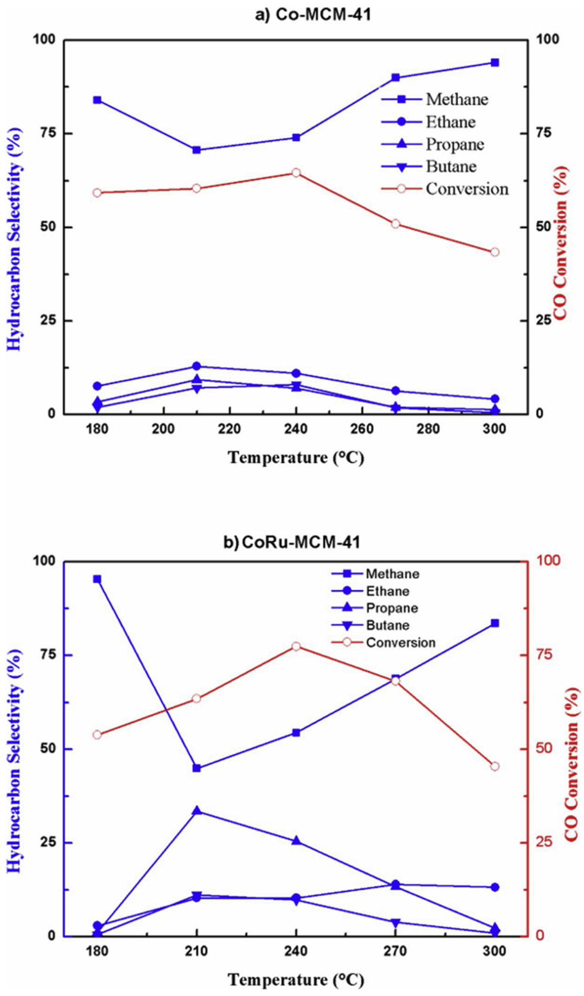

Fig. 12. Effect of temperature on CO conversion and hydrocarbon (C_1-C_4) selectivity: a) Co-MCM-41 b) CoRu-MCM-41 c) CoFe-MCM-41 d) CoNi-MCM-41. (Conditions: H_2/CO = 3:1, P = 1 atm., T = 180 °C, 210 °C, 240 °C, 270 °C, 300 °C)

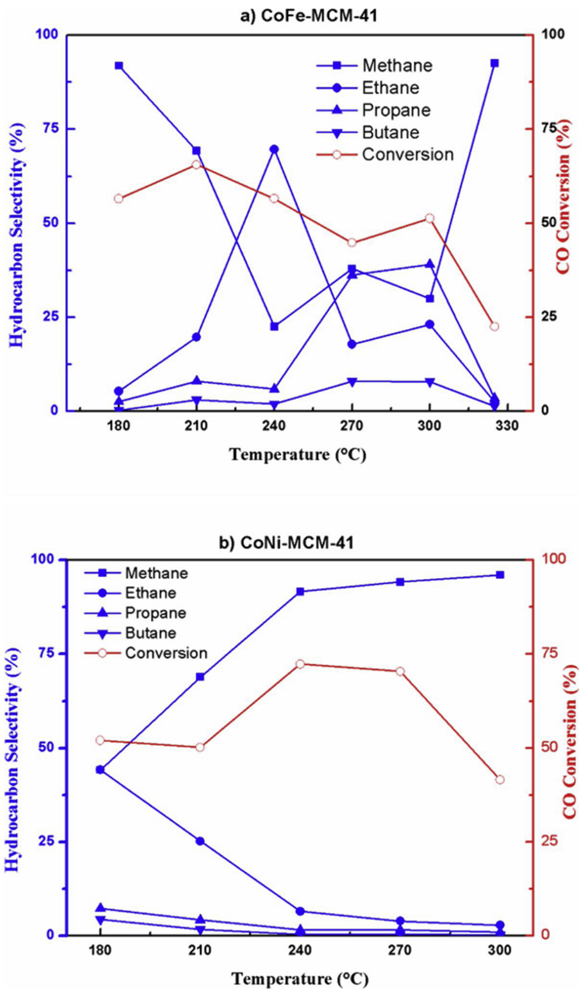

Fig. 13. Effect of temperature on CO conversion and hydrocarbon (C_1-C_4) selectivity a) CoFe-MCM-41 b) CoNi-MCM-41.
(Conditions: H_2/CO = 3:1, P = 1 atm., T = 180 °C, 210 °C, 240 °C, 270 °C, 300 °C for CoNi-MCM-41, T = 180 °C, 210 °C, 240 °C, 270 °C, 300 °C and 325 °C for CoFe-MCM-41.)

methane when compared to the other catalyst under identical conditions. It is well known that Co favors methanation with an increase in the syngas H_2: CO ratio [87]. Since the FT reaction was performed at H_2/CO molar ratio of 3:1, cobalt-based catalyst tends to favor selectivity towards methane at these conditions. The results from our current F–T studies are consistent with our previous work [17], where we investigated F–T synthesis at different temperatures (100 °C–250 °C) with Fe-SiO_2, Co-SiO_2, and Ru-SiO_2, at 1 atm, and H_2/CO ratio of 2 and 3. We observed that Co-SiO_2 catalyst yielded more methane when the H_2/CO mole ratio was changed from 2:1 to 3:1. This is in contrast with Ru-SiO_2 and Fe-SiO_2 catalysts which yielded less amount of methane at 3:1(H_2: CO) molar ratio.

In terms of CO conversion only, Ru exhibited a synergistic behavior in RuCo-MCM-41. More significantly, the effect of a second metal such as Fe, Ru or Ni to Co is clearly manifested in selectivity of hydrocarbons and CO-conversion. The FT reactions mainly produced C_1-C_4, having a low amount of butane that is consistent with the studies reported at 1 atm. [17,18,87]. The selectivity towards methane decreased with increase in the temperature and then increased sharply at the expense of longer chain hydrocarbons at elevated temperatures for all the catalysts. This predominant methane formation relative to ethane, propane, and butane indicates very limited/low polymerization on the active sites. This suggests that the initial surface carbide formation (via CO decomposition) rate is faster than the rate of formation of hydrocarbon chain extenders (−−CH_2−−CH_2 groups), resulting in clogging of metal active sites with carbon deposits. This coking leads to catalyst deactivation and ultimately disrupts polymerization to higher hydrocarbons. The increase in the methane selectivity and decrease in the selectivity towards propane and butane can be attributed to the deposition of carbon on the catalyst from CO decomposition thereby deactivation of the catalyst. The coke formation destroys the chain growth and prevents formation of higher hydrocarbons [18,88,89] at 1 atm.

The other noticeable trend in our FT studies is that CO conversion decreases sharply at higher temperatures from 270 °C to 300 °C. This can be attributed to CO production by reverse water gas shift reaction at higher temperature. Due to the reversible and exothermic nature of the water gas shift reaction [90], the *RWGS* reaction is favored (based on Le Chatelier's principle) at higher temperature. This therefore leads to an elevated concentration of CO and H_2O on the reactant side which results in a high CO to metal active site ratio. Eventually the catalyst active sites become either poisoned by CO or saturated with CO thereby decreasing the fraction of CO that can be converted to products. The highest CO conversion was obtained for the CoRu-MCM-41 catalyst, ~ 74 % at 240 °C. The highest selectivity to butane was 11.2 % for CoRu-MCM-41 at 210 °C and 39 % highest selectivity was associated with the formation of propane for CoFe-MCM-41 at 300 °C.

The CoRu-MCM-41 catalyst exhibited the highest selectivity towards butane among four catalysts studied and the highest selectivity for propane was observed to be 33.5 % at 210 °C with highest CO conversion of 77.4 % at 240 °C. Ruthenium being the most active FT catalyst at lower reaction temperatures, addition of Ru to Co resulted in an increase in the selectivity to higher hydrocarbons.

High temperature (240 − 300 °C) FT (HTFT) activity studies showed that CoFe-MCM-41 catalyst had the highest hydrocarbon selectivity. Particularly at 240 °C, ethane selectivity increased as high as ∼70% while propane selectivity at 300 °C was approximately 40 % while propane selectivity at 300 °C was approximately 40 %; this indeed is the highest among all the studied catalysts. The selectivity of butane was 8% at 270 °C and the catalyst yielded the highest CO conversion of 65.5 % at 210 °C. This high-temperature activity of CoFe-MCM-41 prompted us to further test the performance of the catalyst at 325 °C. However, as shown in Figs. 12 and 13, to our utter dismay, the selectivity of all the hydrocarbons except methane decreased precipitously to approximately 5% at 325 °C. The observed trend is corroborated by the elaborate research work performed by H. Schulz and coworkers in a tubular reactor [91]. Addition of Ni to Co-MCM-41 yielded the highest selectivity for propane and butane at low temperatures and produced almost methane at temperatures > 210 °C. It is reported in the literature that nickel tends to favor methane formation during Fischer Tropsch synthesis [91], and we observed indeed a similar trend with bimetallic CoNi-MCM-41.

In terms of CO conversion, bimetallic CoRu-MCM-41 performed better than monometallic Co-MCM-41, while Co-MCM-41 surpassed bimetallic CoNi-MCM-41and CoFe-MCM-41. This is consistent with the well-known suitability of Co catalysts for FT synthesis. However, in terms of C_1-C_4 selectivity, CoFe-MCM-41, and CoRu-MCM-41 showed significant synergistic behavior and performed better than Co-MCM-41. Conversely, our findings elucidated that the addition of metal promoters (Fe, Ru & Ni) to the Co-MCM-41 play quite distinctive and significant roles in the syngas conversion and C_1-C_4 product distribution at 1 atm.

3.9. Deactivation studies of the catalysts

The catalysts were investigated continuously for 60 h at 240 °C, 1 atm, with H_2/CO ratio of 3:1 in order to ascertain their relative long-term stability and/or their ability to withstand deactivation. The results are shown in Fig. 14. For the first 10 h, all the catalysts maintained a fairly consistent CO conversion in the range of 60–75 %. However, after 20 h they all exhibited a 40 % average CO conversion representing approximately 45 % decline in the CO conversion. The decrease in CO conversion was even more drastic between 20 − 40 hours during which the rate of decline of CO conversion was about 20 % per hour. At the end of 60 h, CoRu-MCM-41 showed complete loss of activity (i.e. no CO conversion), whereas both Co-MCM-41 and CoNi-MCM-41 showed ∼10 % denoting ∼85 % dissipation of CO conversion from the outset of the reaction. Although the loss of activity of CoFe-MCM-41 was also significant, 57 %, it maintained the highest CO Conversion ∼30 % after 60 h. Our observation revealed that in terms of stability, Ru, Fe, and Ni impacted FT performance of cobalt exclusively. More significantly, while Fe addition improved the stability of Co-MCM-41, Ni and Ru substantially decreased the stability of the catalyst as well as CO conversion.

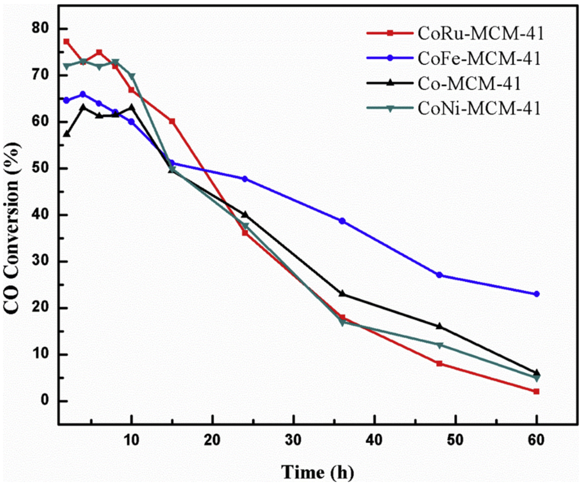

Fig. 14. Deactivation studies of all the catalysts used for FT synthesis. (Conditions: $H_2/CO = 3:1$, P = 1 atm., T = 240 °C).

Addition of Fe, Ni and Ru to the Co-catalyst has shown variation in the deactivation rates possibly due to different deactivation mechanisms of each metal catalyst. Many proposed deactivation mechanisms include catalysts poisoning, sintering, re-oxidation, the effect of water, carbon deposition and surface reconstruction [92]. The syngas used in these studies is a mixture of ultrahigh pure 5.0 CO and H_2 gases; therefore, there is very minimal or no chance of catalyst deactivation due to poisoning by the gas feed. Iglesia et al. reported that the type of support utilized can enhance the ability of the catalyst to resist deactivation [93]. They found that the interaction of cobalt with refractory metal oxides like Al_2O_3 was more stable compared to that of silica. The silica-based MCM-41 support tends to form very stable cobalt silicates over the period of reaction time. This was confirmed by the TPR profile in Fig. 11 in which Co-silicates were reduced at very high temperature > 750 °C and consequently reduced the reactivity of the catalyst. Carbon deposition on the active sites due to coking also played a significant part in the catalyst deactivation which is confirmed by TEM-EDX of the CoRu-MCM-41 shown in Fig. 15. The deactivated CoRu-MCM-41 was also characterized by XPS and TPO (Temperature programmed oxidation) as shown in Figs. S3 and S4 . They confirm the presence of carbon on the surface of the spent catalyst. The deactivation of Fe in CoFe-MCM-41 catalyst is mainly because of water that is produced during the FT synthesis. It reoxidizes Fe to Fe_3O_4 which is inactive during the FT reaction [91]. Although the incorporation of Ru to Co-MCM-41 catalyst has shown clear improvement towards the selectivity of hydrocarbons, Fig. 14 shows that CoNi-MCM-41 is more stable than CoRu-MCM-41 or Co-MCM-41. Ni was found to resist the catalyst deactivation by facilitating reduction by hydrogen spillover [94]. Fan and his coworkers also found that CO conversion increased upon the addition of nickel to cobalt-based catalyst for selective synthesis of wax from syngas [95]. In summary, the stability and activity of the catalysts to withstand/retard deactivation were in the order of CoFe-MCM-41 > Co-MCM-41 > CoNi-MCM-41 > CoRu-MCM-41.

4. Conclusions

In summary, stainless steel microreactors fabricated by 3D-printing technology was successfully used to study the effect of bimetallic M- Co-MCM-41 catalysts in FT synthesis at 1 atm. These catalysts were synthesized using one-pot hydrothermal procedure and resulted in high surface area MCM-41 matrix with an ordered mesoporous structure as -corroborated by low angle XRD and BET surface area studies. TEM and SEM-EDX results indicate a clear hexagonal matrix having porous surface morphology with uniform metal ion distribution. For FT synthesis, all the catalysts showed similar trend in CO conversion. The highest CO conversion for CoFe-MCM-41 (65.5 %), Co-MCM-41 (64 %) and CoNi-MCM-41 (72 %) was obtained at 210 °C, 240 °C and 240 °C respectively, and each of them is lower than that of CoRu-MCM-41 (77.4 %) at 240 °C. The highest selectivity for butane in the temperature range of 180 °C–300 °C followed the order, CoRu-MCM-41 > CoFe-MCM-41 > Co-MCM-41 > CoNi-MCM-41. The selectivity for propane followed the order: CoFe-MCM-41 > CoRu-MCM-41 > Co-MCM-41 > CoNi-MCM-41. Among all the catalysts studied, CoFe-MCM-41 showed the best resistance to deactivation. Monometallic Co exhibited the highest dispersion in the MCM-41framework followed closely by bimetallic Co-Ru. The results from our experiments suggests that the addition of transition metals-Fe, Ni and Ru to Co-MCM-41 can play a vital role in FT

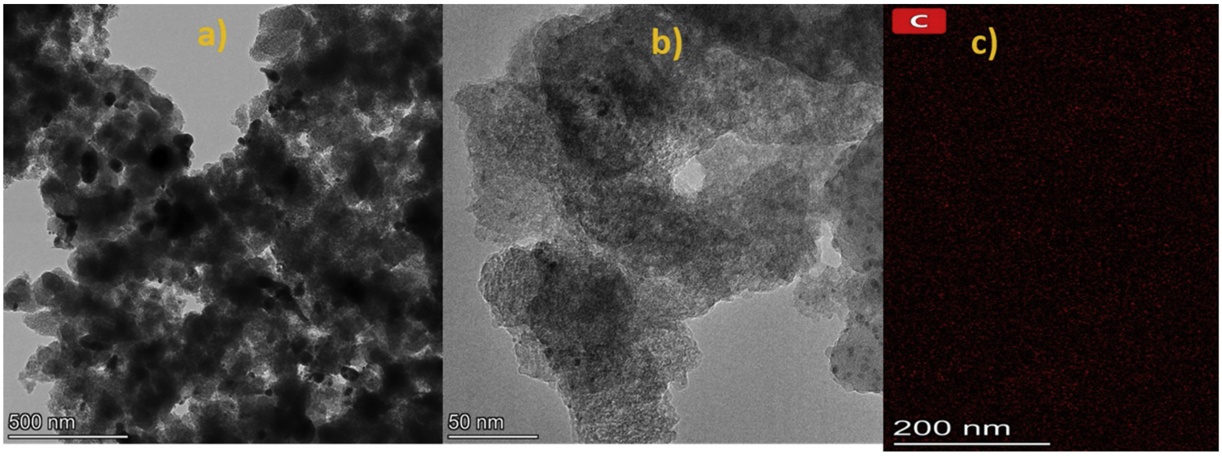

Fig. 15. TEM image of deactivated CoRu-MCM-41 catalyst a) Low magnification b) High magnification c) EDX showing presence of carbon on the catalyst surface.

synthesis. Finally, the 3D-printed stainless steel microreactor enables an ease of catalyst screening and development, addressing major issues that are limited by silicon microreactors.

Acknowledgments

This work is performed at North Carolina A&T State University and Joint School of Nanoscience and Nanoengineering, a member of the Southeastern Nanotechnology Infrastructure Corridor (SENIC) and National Nanotechnology Coordinated Infrastructure (NNCI), which is supported by the National Science Foundation (Grant ECCS-1542174). The authors acknowledge the funding received from NSF-CREST (#260326) and UNC-ROI (#110092). The authors also gratefully acknowledge Dr. Kyle Nowlin and Klint Davis for SEM and TEM support, Dr. Kristen Dellinger for XPS, and Dr. Ramakrishna Sharma for help with the design of microreactor. We thank Prof. Moti Herskowitz of Ben-Gurion University of the Negev, Israel, for useful discussions.

Appendix A. Supplementary data

Supplementary material related to this article can be found, in the online version, at doi:https://doi.org/10.1016/j.cattod.2020.02.020.

References

[1] A.P. Steynberg, Introduction to Fischer-Tropsch technology, Chapter 1, in: A. Steynberg, M. Dry (Eds.), Stud. Surf. Sci. Catal. Elsevier, 2004, pp. 1–63.
[2] O. Glebova, Gas to Liquids – Historical Development and Future Prospects, OIES Paper: NG 80, Oxford Institute for Energy Studies, 2013.
[3] R.C. Brady III, R. Pettit, J. Am. Chem. Soc. 103 (1981) 1287–1289.
[4] R. Guettel, U. Kunz, T. Turek, Chem. Eng. Technol. 31 (2008) 746–754.
[5] A. Pohar, I. Plazl, Chem. Biochem. Eng. 23 (2009) 537–544.
[6] J.J. Lerou, A.L. Tonkovich, L. Silva, S. Perry, J. McDaniel, Chem. Eng. Sci. 65 (2010) 380–385.
[7] V. Hessel, P. Löb, L. Holger, Stud. Surf. Sci. Catal. 159 (2006) 35–46.
[8] X. Ouyang, R.S. Besser, Catal. Today 84 (2003) 33–41.
[9] A. Gavriilidis, P. Angeli, E. Cao, K.K. Yeong, Y.S.S. Wan, Chem. Eng. Res. Des. 80 (2002) 3–30.
[10] R. Myrstad, S. Eri, P. Pfeifer, E. Rytter, A. Holmen, Catal. Today 147 (2009) S301–S304.
[11] X. Ying, L. Zhang, H. Xu, Y.-L. Ren, Q. Luo, H.-W. Zhu, H. Qu, J. Xuan, Fuel Process. Technol. 143 (2016) 51–59.
[12] S. LeViness, S.R. Deshmukh, L.A. Richard, H.J. Robota, Top. Catal. 57 (2014) 518–525.
[13] C. Knobloch, R. Güttel, T. Turek, Chem. Ing. Tech. 85 (2013) 455–460.
[14] F. Asinger, H.M.E. Steiner, Paraffins: Chemistry and Technology, Pergamon Press, 1968.
[15] A. Karim, J. Bravo, D. Gorm, T. Conant, A. Datye, Catal. Today 110 (2005) 86–91.
[16] S. Srinivas, A. Dhingra, H. Im, E. Gulari, Appl. Catal. A Gen. 274 (2004) 285–293.
[17] S. Mehta, V. Deshmane, S. Zhao, D. Kuila, Ind. Eng. Chem. Res. 53 (2014) 16245–16253.
[18] S. Zhao, V.S. Nagineni, N.V. Seetala, D. Kuila, Ind. Eng. Chem. Res. 47 (2008) 1684–1688.
[19] V.S. Nagineni, S. Zhao, A. Potluri, Y. Liang, U. Siriwardane, N.V. Seetala, J. Fang, J. Palmer, D. Kuila, Ind. Eng. Chem. Res. 44 (2005) 5602–5607.
[20] R.Y. Abrokwah, V.G. Deshmane, D. Kuila, J. Mol, Catal. A: Chem. 425 (2016) 10–20.
[21] B. Mueller, Assem. Autom. 32 (2012).
[22] M. Vaezi, H. Seitz, S. Yang, Int. J. Adv. Manuf. Technol. 67 (2013) 1721–1754.
[23] B. Gutmann, M. Koeckinger, G. Glotz, T. Ciaglia, E. Slama, M. Zadravec, S. Pfanner, H. Gruber-Woelfler, M. Maier, C.O. Kappe, React. Chem. Eng. 2 (2017) 919–927.
[24] G. Scotti, S. Nilsson, M. Haapala, T. Kotiaho, Micro Nano Conference, (2016), https://doi.org/10.13140/RG.2.2.19986.96963.
[25] D.-H. Ko, K.-W. Gyak, D.-P. Kim, J. Flow Chem. 7 (2017) 72–81.
[26] M.C. Maier, R. Lebl, P. Sulzer, J. Lechner, T. Mayr, M. Zadravec, E. Slama, S. Pfanner, C. Schmölzer, P. Pöchlauer, C.O. Kappe, H. Gruber-Woelfler, React. Chem. Eng. 4 (2019) 393–401.
[27] R. Myrstad, S. Eri, P. Pfeifer, E. Rytter, A. Holmen, Catal. Today 147 (2009) S301–S304.
[28] S.R. Deshmukh, A.L.Y. Tonkovich, K.T. Jarosch, L. Schrader, S.P. Fitzgerald, D.R. Kilanowski, J.J. Lerou, T.J. Mazanec, Ind. Eng. Chem. Res. 49 (2010) 10883–10888.
[29] Y. Sun, Z. Jia, G. Yang, L. Zhang, Z. Sun, Int. J. Hydrogen Energy 42 (2017) 29222–29235.
[30] B.G. Johnson, C.H. Bartholomew, D.W. Goodman, J. Catal. 128 (1991) 231–247.
[31] O. Borg, S. Eri, E.A. Blekkan, S. Storsæter, H. Wigum, E. Rytter, A. Holmen, J. Catal. 248 (2007) 89–100.
[32] W. Chu, P.A. Chernavskii, L. Gengembre, G.A. Pankina, P. Fongarland, A.Y. Khodakov, J. Catal. 252 (2007) 215–230.
[33] A. Hilmen, D. Schanke, K. Hanssen, A. Holmen, Appl. Catal. A Gen. 186 (1999) 169–188.
[34] S. Storsæter, B. Tøtdal, J.C. Walmsley, B.S. Tanem, A. Holmen, J. Catal. 236 (2005) 139–152.
[35] A. Hilmen, D. Schanke, A. Holmen, Catal. Lett. 38 (1996) 143–147.
[36] F. Morales, F.M. de Groot, O.L. Gijzeman, A. Mens, O. Stephan, B.M. Weckhuysen, J. Catal. 230 (2005) 301–308.
[37] E. Iglesia, S.L. Soled, R.A. Fiato, J. Catal. 137 (1992) 212–224.
[38] J. Li, N.J. Coville, Appl. Catal. A Gen. 181 (1999) 201–208.
[39] T.E. Feltes, L. Espinosa-Alonso, E. de Smit, L. D'Souza, R.J. Meyer, B.M. Weckhuysen, J.R. Regalbuto, J. Catal. 270 (2010) 95–102.
[40] J. Li, G. Jacobs, Y. Zhang, T. Das, B.H. Davis, Appl. Catal. A Gen. 223 (2002) 195–203.
[41] H. Arai, K. Mitsuishi, T. Seiyama, Chem. Lett. 13 (1984) 1291–1294.
[42] D. Duvenhage, N. Coville, Appl. Catal. A Gen. 233 (2002) 63–75.
[43] B. Ernst, S. Libs, P. Chaumette, A. Kiennemann, Appl. Catal. A Gen. 186 (1999) 145–168.
[44] J. Li, G. Jacobs, T. Das, Y. Zhang, B. Davis, Appl. Catal. A Gen. 236 (2002) 67–76.
[45] A. Barbier, A. Tuel, I. Arcon, A. Kodre, G.A. Martin, J. Catal. 200 (2001) 106–116.
[46] Y. Yang, H.-W. Xiang, L. Tian, H. Wang, C.-H. Zhang, Z.-C. Tao, Y.-Y. Xu, B. Zhong, Y.-W. Li, Appl. Catal. A Gen. 284 (2005) 105–122.
[47] G. Moradi, M. Basir, A. Taeb, A. Kiennemann, Catal. Commun. 4 (2003) 27–32.
[48] W. Chen, Z. Fan, X. Pan, X. Bao, J. Am. Chem. Soc. 130 (2008) 9414–9419.
[49] M.C. Bahome, L.L. Jewell, D. Hildebrandt, D. Glasser, N.J. Coville, Appl. Catal. A Gen. 287 (2005) 60–67.
[50] R.M.M. Abbaslou, A. Tavassoli, J. Soltan, A.K. Dalai, Appl. Catal. A Gen. 367 (2009) 47–52.
[51] V.G. Deshmane, R.Y. Abrokwah, D. Kuila, Int. J. Hydrogen Energy 40 (2015) 10439–10452.
[52] R.Y. Abrokwah, V.G. Deshmane, S.L. Owen, D. Kuila, Adv. Mater. Res. 1096 (2015) 161–168.
[53] B. Tatineni, Y. Basova, A. Rahman, S. Islam, M. Rahman, A. Islam, J. Perkins, J. King, J. Taylor, D. Kumar, S. Ilias, D. Kuila, Development of Mesoporous Silica Encapsulated Pd-Ni Nanocatalyst for Hydrogen Production, Production and Purification of Ultraclean Transportation Fuels, American Chemical Society, 2011,

pp. 177–190.
[54] E.P. Barrett, L.G. Joyner, P.P. Halenda, J. Am. Chem. Soc. 73 (1951) 373–380.
[55] K.S. Sing, Pure Appl. Chem. 57 (1985) 603–619.
[56] D. Liu, X.Y. Quek, W.N.E. Cheo, R. Lau, A. Borgna, Y. Yang, J. Catal. 266 (2009) 380–390.
[57] S. Shen, J. Chen, R.T. Koodali, Y. Hu, Q. Xiao, J. Zhou, X. Wang, L. Guo, Appl. Catal. B-Environ. 150-151 (2014) 138–146.
[58] S. Samanta, N.K. Mal, A. Bhaumik, J. Mol, Catal. A: Chem. 236 (2005) 7–11.
[59] F. Adam, T.S. Chew, Open Colloid Sci. J. 5 (2012) 1–4.
[60] N.I. Taib, S. Endud, M.N. Katun, Int. J. Chem. 3 (2011) 2–10.
[61] V.G. Deshmane, Y.G. Adewuyi, Microporous Mesoporous Mater. 148 (2012) 88–100.
[62] A. Derylo-Marczewska, W. Gac, N. Popivnyak, G. Zukocinski, S. Pasieczna, Catal. Today 114 (2006) 293–306.
[63] G.A. Eimer, S.G. Casuscelli, G.E. Ghione, M.E. Crivello, E.R. Herrero, Appl. Catal. A Gen. 298 (2006) 232–242.
[64] C. Huo, J. Ouyang, H. Yang, Sci. Rep. 4 (2014) 1–9.
[65] A. Sterczyńska, A. Deryło-Marczewska, M. Zienkiewicz-Strzałka, M. Śliwińska-Bartkowiak, K. Domin, Langmuir 33 (2017) 11203–11216.
[66] X. Liu, J. He, L. Yang, Y. Wang, S. Zhang, W. Wang, J. Wang, Catal. Commun. 11 (2010) 710–714.
[67] A. De Stefanis, S. Kaciulis, L. Pandolfi, Microporous Mesoporous Mater. 99 (2007) 140–148.
[68] M.C. Biesingera, B.P. Paynec, A.P. Grosvenord, L.W.M. Laua, A.R. Gersonb, R.S.C. Smartb, Appl. Surf. Sci. 257 (2011) 2717–2730.
[69] D. Eliche-Quesada, J. Mérida-Robles, P. Maireles-Torres, E. Rodríguez-Castellón, A. Jiménez-López, Langmuir 19 (2003) 4985–4991.
[70] S.S. Bhoware, A.P. Singh, J. Mol. Catal. A Chem. 266 (2007) 118–130.
[71] S.S. Bhoware, S. Shylesh, K.R. Kamble, A.P. Singh, J. Mol. Catal. A Chem. 255 (2006) 123–130.
[72] Q. Yao, Z.-H. Lu, K. Yang, X. Chen, M. Zhu, Sci. Rep. 5 (2015) 15186-15186.
[73] N. Tsubaki, S. Sun, K. Fujimoto, J. Catal. 199 (2001) 236–246.
[74] G.J. Haddad, J.G. Goodwin, J. Catal. 157 (1995) 25–34.
[75] Ev. Steen, G.S. Sewell, R.A. Makhothe, C. Micklethwaite, H. Manstein, M. de Lange, C.T. O'Connor, J. Catal. 162 (1996) 220–229.
[76] F. Boubekr, A. Davidson, S. Casale, P. Massiani, Microporous Mesoporous Mater. 141 (2011) 157–166.
[77] H. Xiong, Y. Zhang, K. Liew, J. Li, Fuel Process. Technol. 90 (2009) 237–246.
[78] V. Stonkus, K. Edolfa, L. Leite, J.W. Sobczak, L. Plyasova, P. Petrova, Appl. Catal. A Gen. 362 (2009) 147–154.
[79] An. Martínez, C. López, F. Márquez, I. Díaz, J. Catal. 220 (2003) 486–499.
[80] P. Betancourt, A. Rives, R. Hubaut, C.E. Scott, J. Goldwasser, Appl. Catal. A Gen. 170 (1998) 307–314.
[81] N.W. Hurst, S.J. Gentry, A. Jones, Catal. Rev. 24 (1982) 233–309.
[82] Á. Szegedi, G. Pál-Borbély, K. Lázár, React. Kinet. Catal. Lett. 74 (2001) 277–287.
[83] P.B. Amama, S. Lim, D. Ciuparu, Y. Yang, L. Pfefferle, G.L. Haller, J. Phys. Chem. B 109 (2005) 2645–2656.
[84] L.F. Bobadilla, S. Palma, S. Ivanova, M.I. Domínguez, F. Romero-Sarria, M.A. Centeno, J.A. Odriozola, Int. J. Hydrogen Energy 38 (2013) 6646–6656.
[85] D. Liu, X.Y. Quek, W.N.E. Cheo, R. Lau, A. Borgna, Y. Yang, J. Catal. 266 (2009) 380–390.
[86] N. Mohammad, S. Bepari, S. Aravamudhan, D. Kuila, Catalysts 9 (2019) 872.
[87] D. Tristantini, S. Lögdberg, B. Gevert, Ø. Borg, A. Holmen, Fuel Process. Technol. 88 (2007) 643–649.
[88] A. Dinse, M. Aigner, M. Ulbrich, G.R. Johnson, A.T. Bell, J. Catal. 288 (2012) 104–114.
[89] H. Schulz, Top. Catal. 26 (2003) 73–85.
[90] P. Kaiser, R. Unde, C. Kern, A. Jess, Chem. Ing. Tech. 85 (2013) 489–499.
[91] H. Schulz, Appl. Catal. A Gen. 186 (1999) 3–12.
[92] H. Jahangiri, J. Bennett, P. Mahjoubi, K. Wilson, S. Gu, Catal. Sci. Technol. 4 (2014) 2210–2229.
[93] E. Iglesia, Appl. Catal. A Gen. 161 (1997) 59–78.
[94] E. Rytter, T.H. Skagseth, S. Eri, A.O. Sjåstad, Ind. Eng. Chem. Res. 49 (2010) 4140–4148.
[95] L. Fan, K. Yoshii, S. Yan, J. Zhou, K. Fujimoto, Catal. Today 36 (1997) 295–304.